



## **Memo 112**

# **On the SKA Sensitivity and Astrometric Precision under a Turbulent Atmosphere**

I. Martí-Vidal

J.C. Guirado

S. Jiménez-Monferrer

J.M. Marcaide

05/09

# On the SKA Sensitivity and Astrometric Precision under a Turbulent Atmosphere

I. Martí-Vidal<sup>1,2</sup>, J.C. Guirado<sup>1</sup>, S. Jiménez-Monferrer<sup>1</sup>,  
and J.M. Marcaide<sup>1</sup>

<sup>1</sup>*Dpt. Astronomia i Astrofísica, Universitat de València (Valencia, Spain)*

<sup>2</sup>*Max-Planck-Institut für Radioastronomie (Bonn, Germany)*

Draft version 3. Date: 10 May 2009

## Abstract

We present the results of a Monte Carlo study of the astrometric precision and sensitivity of the SKA in snapshot phase-referenced observations. Our simulations consider several effects from the turbulent atmosphere (i.e., ionosphere and wet component of the troposphere) as well as from the antenna receivers. We study the changes in dynamic range and astrometric precision as a function of observing frequency, source separation, and maximum baseline length of the SKA. We find that, for all frequencies between 1 and 10 GHz, sources with flux densities as weak as 100 nJy are well detectable with the SKA from 2-minutes long snapshot observations, provided that a strong calibrator source is located within a few degrees from the target source. We also find that, as expected, the astrometric precision of the SKA decreases as the maximum baseline length decreases, but this is only significant when the atmosphere is not the main limiting factor of the dynamic range of the phase-referenced images.

Our results can also be mapped into a study of source confusion in SKA wide-field observations, given that the random deformations of wide-field images, mostly caused by atmospheric turbulences, have essentially the same origin as the random astrometric variations of phase-referenced sources with respect to the phase center of their calibrators.

## 1 Introduction

It is well-known that ground-based astronomical observations are affected by the atmosphere. Opacity changes produce a bias in the source flux density while dispersive effects distort the shape of the electromagnetic frontwave coming from the source. Such distortion translates into a deformation of the observed source structure and/or a variation of the relative positions of all sources observed in a given field. In the case of astronomical devices based on interferometry, dispersive atmospheric effects can be well modelled if the atmosphere above each element of the interferometer (hereafter, *station*) remains unchanged over the whole portion of the sky being observed. In such cases, the observed visibilities can be calibrated using *antenna-based* algorithms, which are relatively simple and computationally inexpensive.

However, when the spatial variations of the atmosphere are significant within the observed portion of the sky, the opacity and dispersive effects cannot be modeled as a single time-dependent antenna-based complex gain over the field of view. Unless more complicated calibration algorithms are used (e.g., [vdT07]), the effect of these errors on the image are difficult or impossible to fix. In this paper, we report on a study of the effects that a turbulent atmosphere may introduce in SKA observations, covering the full range of SKA frequencies. We will focus our study on the errors introduced by turbulences in the differential astrometry between a strong (calibrator) source and

a weak source located a few degrees away. Our study is numerically equivalent to the study of the deformation of an wide-field SKA image at any point located at a given distance from the center of the field (i.e., the *phase center* of the image), as we will explain later.

We have performed simulations of snapshot phase-referenced SKA observations under the effects of a turbulent atmosphere (ionosphere and wet troposphere) and antenna receivers with a finite temperature. In the next section, we describe the details of the array distribution used, as well as the characteristics of the simulated observations. In Sect. 3, we describe how the synthetic noise coming from the atmosphere and the receivers is added to the visibilities, and describe the procedures followed in our Monte Carlo analysis. In Sect. 4, we present the main results.

## 2 Details of the Simulated Observations

We have simulated a total of 200 SKA stations distributed in the following way: 50% are randomly distributed within a circle of 5 km radius; 25% are distributed outside this circle up to a distance of 150 km, following 5 equiangular spiral arms; the remaining antennae are distributed following the same spiral arms, but up to a distance of 3000 km from the inner circle. The curvature of the Earth's surface has been taken into account, assuming the Earth is a perfect sphere. This approximation is good enough for the purpose of this work. We show the resulting array distribution in Fig. 1. This distribution, following equiangular spiral arms, is similar to those distributions studied by [VLJ08], who investigate the filling factors of such kind of array distributions. This filling factor is then related to the image fidelity of the SKA. We find that this antenna distribution is also optimal for astrometry, since the coverage of the Fourier plane is homogeneous in baseline length and angle. In this work, we do not focus on the the array configuration or the image quality (which will be treated elsewhere), but on the impact that noise from the receivers and the turbulent atmosphere have on the sensitivity and astrometric precision of phase-referenced SKA observations.

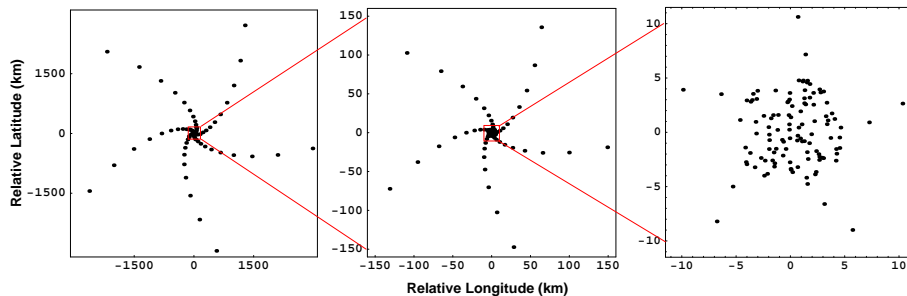


Figure 1: Array configuration used in our simulations. Axes are relative Longitude (horizontal axis) and Latitude (vertical axis) in km. Left, the whole SKA. Center, a zoom to the core. Right, a zoom to the inner core.

### 2.1 Array Sensitivity and Observing Bandwidth

We have simulated SKA observations using 16 different frequencies, which span in logarithmic bins from 150 MHz to 24 GHz. According to [J04], the maximum observing bandwidth of the SKA will be around 25% of the central observing frequency (up to a maximum bandwidth of 4 GHz for all frequencies above 16 GHz). This (maximum) frequency-dependent bandwidth will translate, in our simulations, into a changing sensitivity of the SKA as a function of frequency.

The sensitivities of the SKA stations are also taken from [J04]. These values are set for an elevation of 45 degrees and differ from those given in [SAC07], but the

use of the values given in [SAC07] instead would not affect the main conclusions of this paper. We have interpolated the sensitivities given in Table 1 of [J04] to the frequencies used in our simulations. In Fig. 2 we show the station sensitivities used.

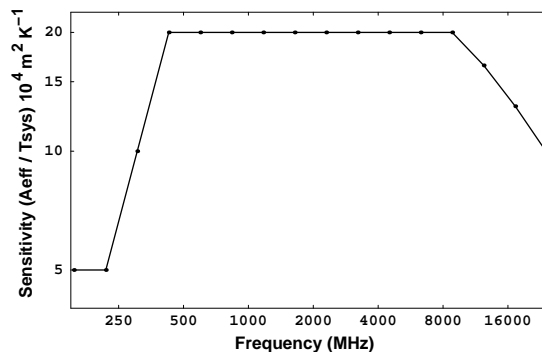


Figure 2: Station sensitivities (i.e., effective areas over system temperatures) used in our simulations.

We have set the target source coordinates at zenith, and an hour angle of 0 degrees for the calibrator. This position of the source minimizes the optical path of the signal through the atmosphere, thus enhancing the quality of the phase-referenced observations. The results given in this paper should be interpreted according to this issue.

### 3 Noise Model

We simulated phase-referencing observations in the following way. We assumed that the calibrator source is sufficiently strong to allow for a perfect antenna-gain calibration at its location. We then determined the quality of the resultant image of the target source (which may be very weak) by simulating the differential antenna-gain errors expected at the target location. These results will depend on the calibrator-to-target separation.

We have simulated two kinds of atmospheric turbulences. The first source of turbulence is associated to the ionosphere (the free electron content, which introduces dispersion in the radiation) and the other source of turbulence is associated to the wet troposphere (the water vapour, close to the earth surface, which is in a state of no thermodynamic equilibrium). The effect of ionospheric turbulences varies as  $1/\nu^2$ , so it mainly affects the low-frequency observations. The effect coming from the wet troposphere varies as  $\nu$ , so it mainly affects the high-frequency observations. The effects coming from the dry troposphere (which is more homogeneously distributed over each station than the wet troposphere) have not been considered in our simulations, given that the differential effects between target and calibrator will be much smaller than those coming from the water vapor and the ionosphere. Models for the turbulences from the ionosphere and troposphere can be found in many publications (e.g., [TMS91]). Here, it is suffice to say that these turbulences follow a Kolmogorov distribution. This distribution has a phase structure function given by:

$$D_\phi(\theta) = \langle (\Phi(\theta_0) - \Phi(\theta_0 + \theta))^2 \rangle \propto \theta^{5/3}$$

where  $\Phi(\theta_0)$  is the phase added by the turbulent screen to the signal of a source located at  $\theta_0$ . The brackets  $\langle \dots \rangle$  represent the averaging over all pointing directions located at a distance  $\theta$  from the point  $\theta_0$ . The Kolmogorov distribution is fractal-like, so both ionosphere and wet troposphere have essentially the same phase distribution, despite of a global factor between them.

The global factors for both distributions (ionosphere and troposphere) are computed according to the typical values of ionospheric and tropospheric conditions. For the ionosphere, the Fried length (i.e., distance in the ionosphere for which the structure function rises to  $1 \text{ rad}^2$ ) is set to 3 km at 100 MHz. For the wet troposphere, we set the parameter  $C_n L$  to  $10^{-11} \text{ m}^{1/3}$  (vid. Eq. 13.100 and Table 13.2 of [TMS91]).

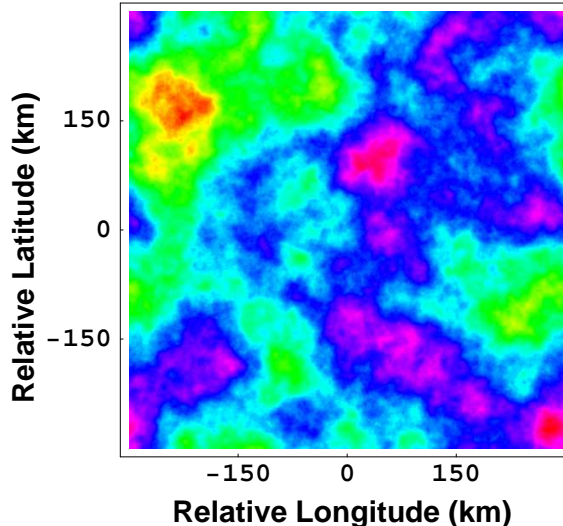


Figure 3: Example of turbulent phase screen with Kolmogorov statistics. The color scale shows relative variations of phases. The absolute values of the phases in the screen will depend (given the self-similarity of this distribution) on a global factor related to the ionospheric and/or wet tropospheric conditions.

We compute the differential effects from the turbulent atmosphere in two ways. For the antennas of the core (within the central 300 km) we generate synthetic phase screens for the ionosphere and troposphere. We show an example of one such screen in Fig. 3. We notice that this figure could represent one of both, either ionosphere or troposphere turbulences in our modelling, just by multiplying the screen by the corresponding scaling factor. Two different screens (one for the ionosphere and the other for the troposphere) are generated in each Monte Carlo simulation. The screen for simulating the ionosphere is put at a height of 300 km and the screen for simulating the troposphere is put at a height of 5 km. For the antennas out of the core, we compute the term  $\Phi(\theta_0) - \Phi(\theta_0 + \theta)$  separately. We proceed this way (i.e., we generate a phase screens only for the core antennas, thus without generating a much larger screen for the whole SKA), because the distances between stations out of the core are large enough to ensure that the cross-correlation of turbulences above different stations will be negligible compared to the correlation between those on the calibrator and target source for the same station. This numerical strategy also speeds up our simulations.

It must be noticed that we do not introduce any time evolution of the turbulent phase screens in our simulations. The shifts and evolution of the turbulences can dramatically affect the observations if the acquisition time is larger than the finite coherence time of the signal, due to the evolution of the turbulences. Such coherence time of course depends on the atmospheric conditions, but also on the observing frequency. However, for snapshot-like observations, of the order of a fraction of a minute or so, we can consider, as a good first approximation, a constant turbulence phase screen.

### 3.1 Receiver Noise Model

Noise from the receivers has been added to our model by generating a random gaussian noise to the real and imaginary parts of the visibilities. Such a noise generates a

Rayleigh distribution for the amplitudes and a uniform distribution for the phases when there is no source observed or its flux density is well below the sensitivity of each baseline. The mean deviation,  $\sigma$ , of the gaussian noise added to the visibilities is (e.g., [TMS91], Eq. 6.43):

$$\sigma = \frac{\sqrt{2} k}{\eta_Q \sqrt{\Delta\nu \Delta t}} \frac{1}{S_A}$$

where  $k$  is the Boltzmann constant,  $\eta_Q$  is the relative loose of signal due to the correlator quantization (we use  $\eta_Q = 0.5$ ),  $\Delta\nu$  is the observing bandwidth,  $\Delta t$  is the observing time, and  $S_A$  is the sensitivity of the stations (collecting area over system temperature, shown in Fig. 2).

## 4 Results

We have simulated sets of different phase-referenced observations. In all cases, the observations are snapshots with a duration of 2 minutes. For each frequency, observations of targets with flux densities of 0.1, 1, and 10  $\mu\text{Jy}$  have been performed with a separation of 5 degrees between target and calibrator. A total of 1500 simulations have been performed for each flux density and frequency. We have chosen such a large separation between calibrator and target, because (as we will see in Sect. 4.2.2) these simulations of phase-referenced observations may also be applied to the study of the deformations of wide-field images under the effects of a turbulent atmosphere. We have also studied the effects of the atmosphere as a function of calibrator-target separation. For that purpose, we have simulated 1500 observations at 1420 MHz (i.e., the Hydrogen line) of a source with 1  $\mu\text{Jy}$  for different separations from the calibrator (2, 3, 4, 5, and 6 degrees).

In all these observations, we have added the noise from the atmosphere and the noise from the receivers. However, in the next subsection we describe the results obtained from simulations without the effects of the atmosphere, which have been performed for a comparison with the theoretical estimates of dynamic range given in [TMS91].

For each simulated phase-reference image, obtained by applying uniform weighting to the visibilities, our program finds the brightness peak and subtracts the corresponding point source from the visibilities. For the subtraction of the point source, the program shifts the brightness peak to the phase center of the image by multiplying the visibilities by the corresponding plane-wave factor in the Fourier plane. Then, the flux density of the point source is estimated as the average of the real part of the resulting visibilities, and the point-source model is subtracted from the data. Afterwards, a Fourier inversion of the new visibilities results in the image of residuals, from which we compute the root-mean-square (rms) of all the pixels. On the one hand, the deviation of the brightness peak with respect to the image center is taken as the astrometry error of that image. On the other hand, the source peak divided by the rms of the residuals is taken as the dynamic range. In Fig. 4 we show the distribution of astrometric deviations and dynamic ranges for the case of a target source of 1  $\mu\text{Jy}$  observed at 1420 MHz (which corresponds to an interferometric beam of  $\sim 13$  mas) located at 5 degrees from the calibrator. Once the distributions like those shown in Fig. 4 have been obtained, we compute the standard deviation of astrometric corrections and the mean value of dynamic ranges for each source flux density, frequency, and separation. The first quantity is an estimate of the astrometric uncertainty, and the second quantity is an estimate of the achievable dynamic range.

In the next subsections, we present the main results obtained from all these simulations.

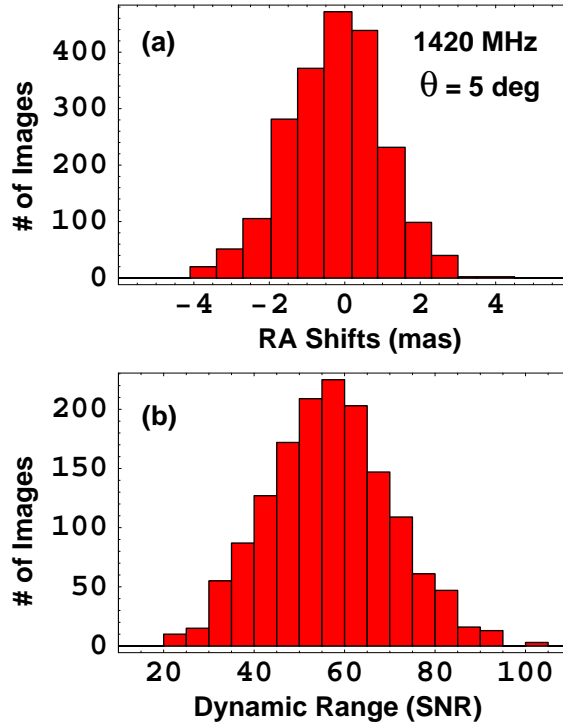


Figure 4: Distribution of right ascension shifts (a) and dynamic ranges (b) of 1500 snapshot phase-referenced images, simulated at 1420 MHz with a target source flux density of  $1 \mu\text{Jy}$ .

#### 4.1 Simulations without Atmosphere

For the case of atmosphere-free simulations, we obtain the astrometric uncertainties and mean dynamic ranges shown in Fig. 5. The points with dynamic ranges below  $\sim 10$  should be considered as non-detections of the target (we could be mostly detecting, in these cases, spurious noise peaks). The dynamic ranges obtained depend on flux density and observing bandwidth in the same way as the theoretical predictions given by [TMS91] (see their Eq. 6.53). When the source is well detected (as it is the case, for instance, of a  $10 \mu\text{Jy}$  source observed at all frequencies), we find that the source is perfectly centered in all the phase-referenced images, regardless of their angular size. This means that, given a dynamic range large enough (i.e., larger than  $\sim 100$ , see Fig. 5) the noise from the receivers, itself, does not introduce any effective uncertainty to the astrometry. Indeed, we could take, as an estimate of the uncertainty, the diffraction limit of the interferometer (i.e., one half of the beam size) divided by the dynamic range of the images. The uncertainties estimated this way are unrealistically small for a target-calibrator separation of 5 degrees (only a few tens of  $\mu\text{as}$ ). For these particular cases, in Fig. 5 we have taken one half of the pixel size as an estimate of the astrometric uncertainty. Since our software uses the same image size (relative to the beam size) for all frequencies, and we need to make the images large enough to be able to compute the astrometric error in the worse cases, one half of the size of a pixel has been taken as 0.17 times the interferometric beam (for an image size of  $1024 \times 1024$  pixels). This corresponds to a beam size of  $\sim 3$  pixels. This choice of a pixel size is arbitrary, so Fig. 5 (and, especially, the astrometric uncertainties corresponding to dynamic ranges greater than  $\sim 100$ ) should be interpreted accordingly.

These simulations without atmospheric effects are unrealistic and the results obtained are not important for the purpose of this paper. The main reason to perform these simulations was to compare the resulting dynamic ranges with the theoretical estimates given by Eq. 6.53 of [TMS91], as a test of our software. Nevertheless, an extra conclusion has been also obtained: the noise from the receivers (which is uncorrelated between antennas) does not introduce any systematics in the phases, which

results in null variations of the positions of the sources provided the dynamic ranges are high enough (i.e., above  $\sim 100$ ).

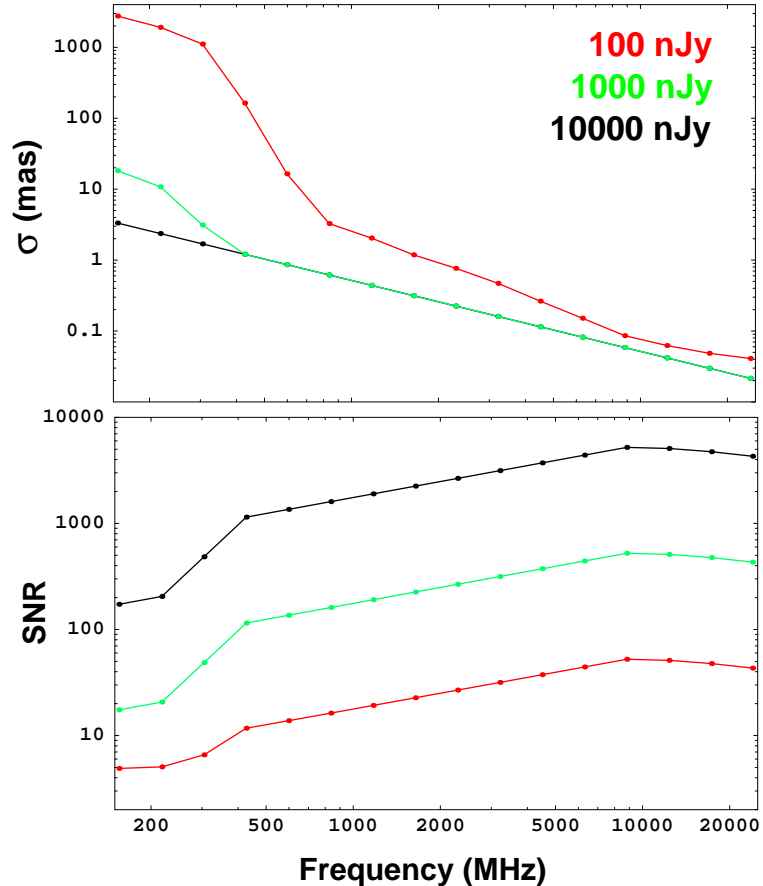


Figure 5: Astrometric accuracy (a) and dynamic range (b) as a function of frequency, for the case with no atmospheric turbulences (i.e., only with the noise coming from the receivers) and a separation of 5 degrees between calibrator and target. Different colors correspond to different target source flux densities (0.1  $\mu$ Jy in red, 1  $\mu$ Jy in green, 10  $\mu$ Jy in black).

## 4.2 Simulations with Atmosphere

When a turbulent ionosphere and wet troposphere are added to the simulations, we obtain the astrometric uncertainties and dynamic ranges shown in Fig. 6. For very low frequencies (below  $\sim 500$  MHz) the ionosphere avoids a clear and precise detection of all sources, no matter their flux densities. For higher frequencies, the astrometric uncertainty decreases notably (mainly because of the dependence of ionospheric effects with  $\nu^{-2}$ ) and gets limited only by diffraction and sensitivity between 1 and 10 GHz (this frequency window slightly depends on the source flux density, as it can be seen in the figure). For higher frequencies, the wet troposphere begins to affect the astrometric uncertainty, which rises up to around 10 mas for the highest frequencies. We find that the best astrometric accuracy, at least for reasonably well-detected sources, is achieved for frequencies around 4 GHz. This is where the ionospheric and (wet) tropospheric components are roughly equal.

The dynamic range of the phase-referenced images is highly limited by the atmosphere. If there was no atmosphere, the dynamic range would be proportional to the flux density of the observed source, so it would have no theoretical limitation. However, when the atmosphere adds noise to the visibility phases (which is not related to the visibility amplitudes) there is an extra rms added to the residual images, which



Figure 6: Astrometric accuracy (a) and dynamic range (b) as a function of frequency, for the case with atmospheric turbulences and a separation of 5 degrees between calibrator and target. Different colors correspond to different target source flux densities ( $0.1 \mu\text{Jy}$  in red,  $1 \mu\text{Jy}$  in green,  $10 \mu\text{Jy}$  in black).

will depend on the visibility amplitudes, thus limiting the achievable dynamic range no matter the flux density of the source. In other words, if the source flux density is higher, the noise of the image will also be higher. This limitation is, of course, more important for the brightest sources. In our case, the brightest source has a flux density of  $10 \mu\text{Jy}$ . For this source, the maximum dynamic range achieved (corresponding to an observing frequency of 3.2 GHz) is only 110. The dynamic range at the same frequency for the case without atmosphere arrives to 3200 (i.e., a factor  $\sim 30$  larger). This situation can be also understood in another way: the rms of the final image is divided into two components, which are added in quadrature. One component comes from the receiver noise and is independent of the source flux density. The other component comes from the atmospheric refraction and is equal to a percentage of the source flux density.

#### 4.2.1 Angular Separation and Signal Decoherence

The results shown in the previous subsection correspond to a separation of 5 degrees between source and calibrator. This situation changes when the angular separation changes. We have computed astrometric uncertainties and dynamic ranges for a source with a flux density of,  $1 \mu\text{Jy}$ , located at 2, 3, 4, 5, and 6 degrees from its calibrator. Noise coming from the atmosphere and the receivers has been taken into account in these simulations. We have used an observing frequency of 1420 MHz (the Hydrogen line) which is inside the frequency window where the atmospheric effects

are minimised. Therefore, all the astrometric errors derived are small (of the order of a few mas), allowing us to use image sizes small enough to sample the beam with more pixels ( $\sim 30$  pixels) using a grid of  $1024 \times 1024$  pixels. This fine gridding of the beam allows for a more accurate determination of the location of the image peak and, therefore, of the estimate of the astrometric error. The results obtained are shown in Fig. 7. In that figure, we also plot two analytical (phenomenological) models for the estimate of the increase of astrometric uncertainty and the loose of dynamic range (i.e., degree of signal decoherence) as a function of angular separation. On the one hand, the phenomenological model proposed for the estimate of loose of dynamic range is:

$$D = \frac{D_0}{k \theta^\beta + 1}, \quad (1)$$

where  $D$  is the dynamic range,  $\theta$  is the angular separation between target and calibrator,  $D_0$  is the dynamic range without atmosphere (i.e., when the calibrator-target separation,  $\theta$ , tends to 0), and  $k$  and  $\beta$  are two dimensionless parameters related to the atmospheric conditions, source flux density, and observing frequency. This equation is derived from the fact that the points shown in Fig. 7(b) are quasi-linear if plotted in log-log space (so there must be a power-law relation between  $D$  and  $\theta$ ), but we should obtain  $D_0$  when  $\theta = 0$ . As it can be seen, this model fits very well to the simulations. We fit  $k = 0.48 \pm 0.04$  and  $\beta = 1.04 \pm 0.06$ .

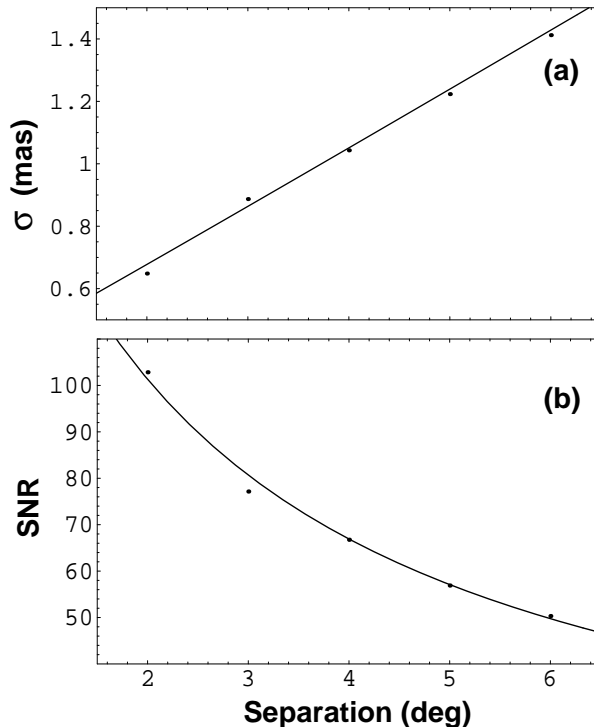


Figure 7: Dots: simulated astrometric accuracy (a) and dynamic range (b) as a function of angular separation between calibrator and source, for observations at 1420 MHz and a target flux density of  $1 \mu\text{Jy}$ . Lines: proposed phenomenological models.

On the other hand, the proposed phenomenological model for the increase of astrometric uncertainty is:

$$\sigma = \frac{\sigma_0}{D_0} (k' \theta^{\beta'} + 1), \quad (2)$$

where  $\sigma$  is the astrometric uncertainty,  $\sigma_0$  is the diffraction limit (i.e., half the size of the beam), and  $k'$  and  $\beta'$  are two dimensionless parameters also related to the atmospheric conditions, source flux density, and observing frequency. The reasons for proposing this model are essentially the same as for the model of the loose of dynamic range. We fit  $k' = 0.57 \pm 0.04$  and  $\beta' = 1.02 \pm 0.05$ . We notice that our results are qualitatively similar to those reported in [PCL06], who found a dependence on  $\sigma$  proportional to  $\theta$  for simulated phase-reference observations with the VLBA and the EVN. Nevertheless, our approach in the treatment of the noise coming from the atmosphere is completely different than that used in [PCL06].

We notice that if we change  $D_0$  by  $D$  in Eq. 2, the new fitted  $k'$  and  $\beta'$  are  $1.03 \pm 0.09$  and  $0.07 \pm 0.06$ , respectively. This new value of  $\beta'$  is compatible with zero. In other words, the diffraction limit divided by the dynamic range of the image is an excellent estimator of the astrometric uncertainty, at least for the range of simulated calibrator-target separations.

#### 4.2.2 Atmospheric Restrictions for SKA Wide-Field Imaging

Our Monte Carlo study can also be applied to the study of atmospheric effects on wide-field imaging, given that the deformation produced by the atmosphere in a wide-field image at a distance  $\theta$  from its phase center has the same origin as the astrometric variation of phase-referenced observations of sources separated by a distance  $\theta$ . The same direct comparison can be made between the (local) dynamic range of the wide-field image and the dynamic range of the phase-referenced image. In both cases, the differential phases introduced by the atmosphere between both pointing directions are the same for each baseline, so the effects in Fourier space (and therefore in the sky plane) will also be the same.

In that sense, the wide-field images taken with the SKA would have random deformations and local dynamic ranges which would depend on the separation from the image phase center according to the analytical models proposed in the previous subsection. For the frequencies (and flux densities) for which the atmospheric effects are minimum (see Fig. 6) such image deformations would also be minimum, but outside that range of frequencies (and flux densities) the atmospheric effects may introduce strong deformations and local losses of sensitivity in the wide-field images.

### 4.3 Maximum Baseline Length

We have repeated all our simulations stretching the whole array distribution by a factor 2 (i.e., decreasing all the baseline lengths to a halfth of their initial values). We find that, as we would expect, the diffraction limit (the size of the interferometric beam) is multiplied by the same stretching factor. In Fig. 8 we show the ratios of astrometric precision and dynamic range between the images obtained with the stretched array and those obtained with the original array. As it can be seen, the dynamic ranges of the images obtained with the compact (stretched) array are slightly higher (around 10-20% higher, depending on frequency and source flux density). This increase in dynamic range contributes to an increase in the astrometry precision that tends to compensate, in some cases, the diffraction-limit difference between both arrays, specially when the effects of the atmosphere are strong.

## 5 Conclusions

We report on Monte Carlo estimates of the sensitivity and differential astrometric precision of a specific realization of the SKA as a function of observing frequency, flux density, and source separation. Our estimates are based on simulations of snapshot phase-referenced observations, in which we take into account several effects from the turbulent atmosphere and the finite temperature of the receivers. We find that the astrometric uncertainty strongly depends on the observing frequency and smoothly increases as the source separation increases. For frequencies below  $\sim 1$  GHz, ionospheric

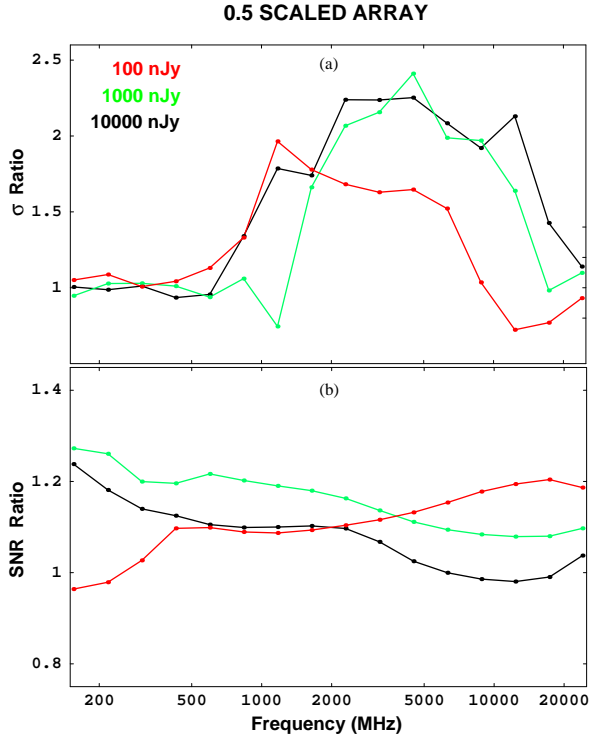


Figure 8: Ratios of the astrometric accuracy (a) and the dynamic range (b), of the images obtained from a stretched version of the array described in Sect. 2 and those obtained from such array. The stretched array is 50% smaller than the original one. Different colors correspond to different target source flux densities ( $0.1 \mu\text{Jy}$  in red,  $1 \mu\text{Jy}$  in green,  $10 \mu\text{Jy}$  in black).

effects dominate and the astrometry uncertainties (when the source is detectable) can be as large as  $\sim 1$  as. For frequencies between 1 and 10 GHz (these values slightly depend on the source flux density) atmospheric effects are minimum and we roughly reach the theoretical precision of the interferometer. Above these frequencies, the wet troposphere begins to dominate and the astrometry precision decreases to  $\sim 10$  mas for the highest frequency (25 GHz). The dynamic range of the images is strongly limited by atmospheric turbulences at all frequencies and for all flux densities (it can decrease, in the worse cases, several orders of magnitude compared to the cases with no atmosphere).

Stretching the whole array by a given factor does not affect the astrometry precision by the same factor, given that the higher dynamic ranges obtained with the more compact arrays tend to compensate the difference in diffraction limits. This is specially true when the effects of the atmosphere are important, depending on the observing frequency and/or source flux density.

We propose analytical models for the loss of dynamic range and astrometric accuracy as a function of distance between calibrator and target source. These expressions could also be used to estimate the deformations and local dynamic ranges of wide-field images as a function of distance to the phase center (i.e., the point where the data correlation is centered).

### Acknowledgements

We thank Ed Fomalont for his very useful comments and suggestions. This work has been supported by the European Community Framework Programme 6, Square Kilometre Array Design Studies (SKADS), contract number 011938. This work has also been partially founded by grants AYA2006-14986-CO2-01 and AYA2005-08561-C03 of the Spanish DGICYT. IMV is a fellow of the Alexander von Humboldt Foundation.

## References

- [E98] Eckers R.D., 1999, in *Synthesis Imaging in Radio Astronomy II* (Taylor, Carilli & Perley, eds.), ASP Conference Series Vol. 180
- [J04] D.L. Jones, 2004, SKA Memo 45
- [PCL06] Pradel N., Charlot, P., & Lestrade J.-F., 2007, *A&A*, 452, 1099
- [SAC07] R.T. Schilizzi, P. Alexander, J.M. Cordes, P. E., et al., 2007, SKA Memo 100
- [TMS91] A.R. Thomson, J.M. Moran, and G.W. Swenson, *Interferometry and Synthesis in Radio Astronomy*, 1991, Krieger Publ. Corp. (Florida)
- [vdT07] S. van der Tol, B.D. Jeffs, and A.J. van der Veen, 2007, in *IEEE Tr. Signal Processing*
- [VLJ08] D. Vir Lal, A.P. Lobanov, and S. Jiménez-Monferrer, 2008, SKA Memo (in preparation)